Automation in Construction 133 (2022) 104004

Contents lists available at ScienceDirect

Automation in Construction

journal homepage: www.elsevier.com/locate/autcon

Detection of delamination and rebar debonding in concrete structures with ultrasonic SH-waveform tomography

Ruoyu Chen [a], Khiem T. Tran [a,*], Hung Manh La [b], Taylor Rawlinson [a], Kien Dinh [c]

[a] Department of Civil & Coastal Engineering, University of Florida, Gainesville, FL, USA
[b] Department of Computer Science and Engineering, University of Nevada, Reno, NV, USA
[c] NDT Concrete LLC, FL, USA

ARTICLE INFO

Keywords:
Concrete inspection
Delamination
Rebar debonding
Ultrasonic FWI
SH- and love-waves

ABSTRACT

The detection of delamination and rebar debonding is among the most frequently encountered issues for inspecting concrete for quality control and assurance. This paper presents a novel application of a 2D full-waveform inversion of ultrasonic SH-waves (SH-FWI) for detection of delamination and rebar debonding in concrete structures. The ultrasonic data are collected by a commercial shear-wave tomography device (MIRA) and analyzed by the SH-FWI method to extract the material properties (density and S-wave velocity) at mm-resolutions. Tested on a concrete slab with four delaminations of various sizes and depths and rebar debonding, the method was able to characterize all delaminations at accurate location and sizes, as well as identify the existence of rebar debonding. Compared to the synthetic aperture focusing technique (SAFT), the SH-FWI method provided clearer structural images with more detailed information of the delamination and rebar debonding.

1. Introduction

Concrete delamination and steel bar debonding are among the most common types of defects in reinforced concrete structures [1–3]. The primary causes of formation of these defects are either the corrosion of steel bar due to the presence of soluble chlorides [1,2], or the overloading of the structure [3]. The corrosion of steel will first create a rust layer surrounding the rebar, which will result in the loss of the cohesion (debonding) between that bar and concrete. Later, the volumetric expansion of such rust layer will initiate internal cracks, which will then develop and connect to those from neighboring rebars to form the so-called concrete delamination [2]. With respect to overloading, a relative sliding between concrete and steel bar will occur once the shear stress at the steel/concrete interface become greater than the shear strength that helped hold them together [3].

Regardless of the cause of formation, both delamination and rebar debonding will ultimately reduce the integrity of reinforced concrete structures and affect their ability to withstand the applied loads [2]. These types of defects have been intensively studied because of the following reasons. First, from the users' point of view, structure owners are held accountable for any safety issues of their structures. As a result, they often desire to know all types of defects in the structures if any of them exists. Second, from the economic point of view, the early detection of defects within a structure will help its owner to identify the most cost-effective course of maintenance actions. For example, while the active rebar corrosion within a specific bridge deck does not indicate an imminent bridge collapse, a knowledge of its existence will help the corresponding transportation agency to identify the most appropriate repair action/plan for that bridge deck. All being said, the ultimate goal of this study was to develop an accurate method for the detection of delamination and rebar debonding in concrete.

Various nondestructive testing (NDT) methods have been developed and employed for the detection of delamination and rebar debonding in reinforced concrete structures. They include ground penetrating radar (GPR) [4,5,6,7,8], impact echo (IE) [9,10,11,7,12,13], or ultrasonic array techniques [14,15,10,11]. It has been observed that that each of these technologies has advantages and limitations. For example, concerning GPR, a recent study [16] suggested that the GPR has difficulty in detecting thin air-filled delamination due to the destructive interference of closely reflected signals; or it can hardly detect deep delamination due to signal attenuation and mixed waveforms between those from dense rebars and back-wall boundary. With respect to the IE method, while it

* Corresponding author.
E-mail addresses: chen.ruoyu@ufl.edu (R. Chen), ttk@ufl.edu (K.T. Tran), hla@unr.edu (H.M. La), taylor.rawlinson@essie.ufl.edu (T. Rawlinson), kien@ndt-concrete.com (K. Dinh).

https://doi.org/10.1016/j.autcon.2021.104004
Received 15 July 2021; Received in revised form 4 October 2021; Accepted 6 October 2021
Available online 19 October 2021

can provide the indication of concrete delamination, it is not able to accurately visualize such defects in 2D or 3D spaces. Furthermore, there have been no studies on the use of IE technique for detection of rebar or rebar debonding. As for the ultrasonic array measurements, the commonly used equipment is the MIRA device with the built-in software based on the synthetic aperture focusing technique (SAFT). A previous study [14] concluded that while the MIRA and its built-in SAFT can provide a clear visualization of concrete delamination, it cannot detect steel bar/concrete debonding.

Using the complete recorded wavefields, the full-waveform inversion (FWI) is a promising approach for detection of concrete structural defects at high resolutions. Substantial development of FWI has been made in the past two decades [17], for material imaging at various scales from meters to kilometers (e.g., 2D FWI: [18,19,20,21,22], and 3D FWI: [23,24,25,26,27]). FWI algorithms have also been applied for NDT at smaller scales of millimeters to decimeters [28,29,30] and for imaging of concrete bridge abutments [31,32] and decks [33]. Most of these FWI studies focused on inversion of P- and S-waves (P-SV waves). Recently, the SH- and Love-wave inversion has gained more attention [34,35,36,37,38], since it has the advantage of higher sensitivity to S-wave velocity (Vs) and mass density than the P-SV wave inversion. To our best knowledge, the SH-FWI has not been applied for detection of damages in reinforced concrete structures.

In this study, we apply a recently developed 2D SH-FWI method [39] on ultrasonic wavefields for detecting delamination and rebar debonding in concrete structures. The ultrasonic data are collected using a shear-wave tomography device (A1040 MIRA), which uses dry point contact (DPC) transducers. This portable device is selected because of its convenient operation and the rich ultrasonic information in collected waveform data [14]. The method's capability is examined on a fabricated concrete slab, which includes rebars, artificial delaminations and rebar debonding of various severity. The SH-FWI result is also compared with the conventional synthetic aperture focusing technique (SAFT) [40].

2. Research methodology

The 2D SH-FWI method has recently been developed for the geotechnical characterization at meter-scales [39], with its algorithm written in MATLAB. The method consists of the forward modelling using 2D elastic SH-wave equations and model updating using the adjoint-state method with Tikhonov regularization. Through the iterative model updating, material properties Vs and mass density are extracted in the test domain. The method is briefly summarized herein for inversion of ultrasonic data.

For the forward modelling, the time-domain finite-difference method [41] was used to solve 2D SH-wave equations to simulate ultrasonic wavefields as:

$$\rho(x,z)\frac{\partial v_y}{\partial t}=\frac{\partial \sigma_{xy}}{\partial x}+\frac{\partial \sigma_{yz}}{\partial z}+f_y \tag{1}$$

$$\frac{\partial \sigma_{xy}}{\partial t}=\mu(x,z)\frac{\partial v_y}{\partial x} \tag{2}$$

$$\frac{\partial \sigma_{yz}}{\partial t}=\mu(x,z)\frac{\partial v_y}{\partial z} \tag{3}$$

where $\rho(x,z)$ is the mass density, $\mu(x,z)$ is the shear modulus, v_y is the particle velocity, σ_{xy} and σ_{yz} are shear stresses, and f_y is the applied force (source) in y-direction. At the top boundary of the modelled domain, the free surface condition was applied through the stress-imaging technique [42]. At the side and bottom boundaries of the domain, the perfectly matched layers [43] were applied to absorb outgoing waves for boundary truncation.

The residual between estimated and observed ultrasonic waveforms is calculated as:

$$\Delta \boldsymbol{d}_{t,r}=\boldsymbol{D}_{t,r}(\mathbf{m})-\boldsymbol{d}_{t,r}, \tag{4}$$

where $\mathbf{m}$ represents the model parameters (i.e., Vs and density of cells). $\boldsymbol{D}_{t,\,r}(\mathbf{m})$ denotes the estimated ultrasonic data corresponding to model $\mathbf{m}$, generated from the forward modelling, and $\boldsymbol{d}_{t,\,r}$ denotes the measured ultrasonic data from the MIRA device. The subscripts t, r represent the t-th transmitter (source) and the r-th receiver. The objective function is then computed as the least-squares error:

$$\mathrm{E}(\mathbf{m})=\frac{1}{2}\Delta \boldsymbol{d}^{\mathrm{T}}\Delta \boldsymbol{d}, \tag{5}$$

where $\Delta \boldsymbol{d}$ is a column vector, which includes the residuals $\Delta \boldsymbol{d}_{t,\,r}$ from all transmitters and receivers. T represents the vector transpose.

The objective function is minimized by following a search direction (gradient). The gradients of the objective function with respect to Vs and density are computed based on the adjoint-state method [44] as:

$$\frac{\partial E}{\partial V_s}=-\frac{2}{V_s^3\rho}\sum_{i=1}^{N}\int_0^T dt\left(\sigma_{xy}^f\sigma_{xy}^b+\sigma_{yz}^f\sigma_{yz}^b\right), \tag{6}$$

$$\frac{\partial E}{\partial \rho}=-\frac{1}{V_s^2\rho^2}\sum_{i=1}^{N}\int_0^T dt\left(\sigma_{xy}^f\sigma_{xy}^b+\sigma_{yz}^f\sigma_{yz}^b+V_s^2\rho^2\frac{\partial v_y}{\partial t}u_y^b\right), \tag{7}$$

where N is the number of transmitters, $\sigma_{xy}{}^f$, $\sigma_{yz}{}^f$ and v_y represent the shear stresses and particle velocity of the forward-propagated wavefield, respectively. Parameters $\sigma_{xy}{}^b$, $\sigma_{yz}{}^b$ and $u_y{}^b$ represent the shear stresses and particle displacement of the back-propagated wavefield by propagating residuals from receiver locations, respectively. Tikhonov regularization [45] is then applied to regularize the gradients:

$$\left(\frac{\partial E}{\partial V_s}\right)_r=\frac{\partial E}{\partial V_s}+\lambda_1 \boldsymbol{D}V_s \tag{8}$$

$$\left(\frac{\partial E}{\partial \rho}\right)_r=\frac{\partial E}{\partial \rho}+\lambda_2 \boldsymbol{D}\rho \tag{9}$$

where D is the 2D Laplacian matrix, whose elements are either 1, −4 or 0. The size of matrix D is N × N, where N is the number of the reconstructed parameters or cells. Coefficients λ_1 and λ_2 represent the scaling factors between the regularization term and the gradient term. See [39] for more detailed implementation.

The Vs and density models are updated iteratively along the steepest-descent directions [46] as:

$$V_{sn+1}=V_{sn}-\alpha_n \boldsymbol{H}_n^{-1}\left(\frac{\partial E}{\partial V_s}\right)_r, \tag{10}$$

$$\rho_{n+1}=\rho_n-\beta_n \boldsymbol{H}_n^{-1}\left(\frac{\partial E}{\partial \rho}\right)_r, \tag{11}$$

where α_n and β_n are the optimal step lengths and obtained independently via parabolic fitting. $\boldsymbol{H}_n{}^{-1}$ is the inverse of Hessian matrix and its approximation [47] is adopted as:

$$\boldsymbol{H}_n^{-1}=\left\{\lambda+\sqrt{W_t(\boldsymbol{x},x_t)W_r(\boldsymbol{x})}\right\}^{-1}, \tag{12}$$

where

$$\lambda=0.1\,max_x\left\{\sqrt{W_t(\boldsymbol{x},x_t)W_r(\boldsymbol{x})}\right\}, \tag{13}$$

where x_t denotes the location of transmitter. $W_t(\boldsymbol{x},x_t)$ and $W_r(\boldsymbol{x})$ represents the energies of the forward-propagated wavefield and the back-propagated residual wavefield at location $\boldsymbol{x}=[x,z]$, respectively. Factor λ is used to avoid the inverse of infinitesimals. Finally, the inversion analysis stops when the predefined maximum number (30) of iterations is reached, or the models cannot be improved (no optimal step lengths

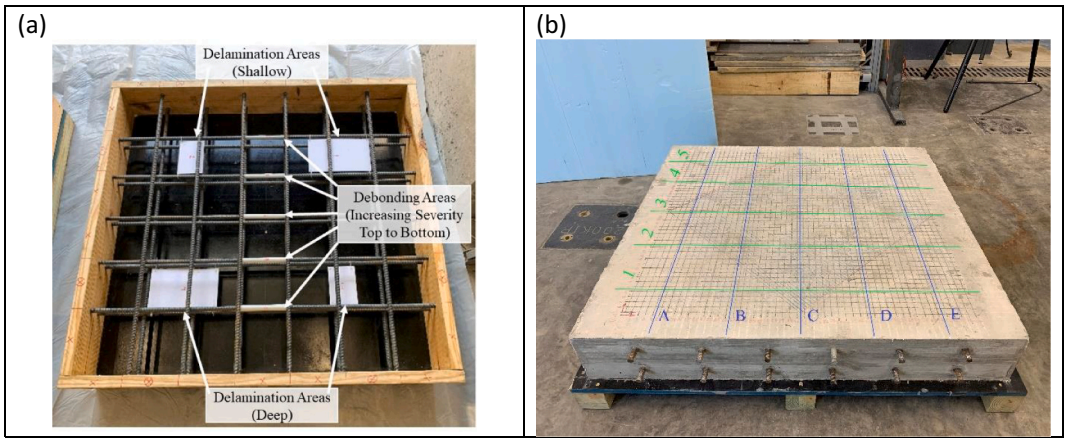

Fig. 1. The concrete slab specimen: (a) formwork used for concrete slab casting, and (b) finished concrete slab.

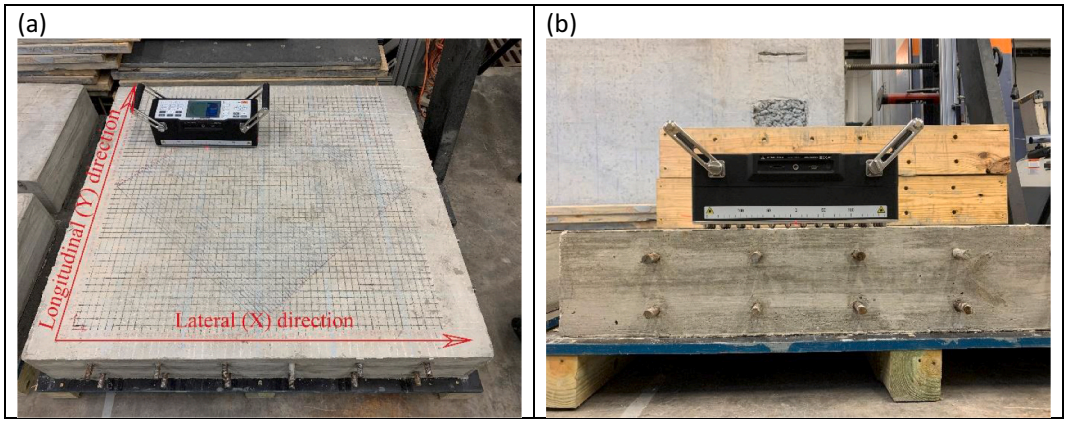

Fig. 2. The MIRA used for data sampling: (a) top view, and (b) side view.

are found).

3. Experimental setup

The 2D SH-FWI method was validated on a concrete slab fabricated in the Weil Hall Structures and Materials Laboratory at the University of Florida in Gainesville, Florida (USA). The formwork was designed and prepared for casting as shown Fig. 1a. It included standard Grade 40 rebar, four delamination areas, and five debonding areas. A total of 22 rebars of the same size (#5, US/Imperial) were installed in two orthogonal directions, 12 rebars in one direction and 10 rebars in the other direction. In each direction, the rebars were placed as two parallel layers as top and bottom steel. To simulate delaminations at various severity, four foam core backing boards of differing sizes and thicknesses were tied to the rebars at two depths of 65 mm and 130 mm (Fig. 1a). Two foams of 100 × 150 × 3 mm (upper, left) and 250 × 150 × 3 mm (upper, right) were embedded at a shallow depth of 65 mm. Two other foam areas of 250 × 150 × 6 mm (bottom, left) and 100 × 150 × 9 mm (bottom, right) were embedded at a deeper depth of 130 mm. To simulate the rebar debonding, the middle section of each lateral top rebar was coated with multiple rolls of tightly wrapped 4-mil visqueen plastic prior to the casting. As shown in Fig. 1a, from top to bottom, the number of rolls is two, four, six, eight, ten, respectively, to represent different severity of debonding. The cover depths for five debonding rebars vary from 56 mm to 58 mm. A high-slump concrete was cast and vibrated to ensure appropriate consolidation around foam delamination areas and rebar. The concrete was finished with a magnesium bull float to ensure a smooth surface for scanning device contact points. After removal of the formwork, the fabricated concrete slab had the dimension of 1220 × 1150 × 190 mm. It was marked for the experiment as shown in Fig. 1b.

Ultrasonic wave data were generated and collected by the commercial shear-wave system (A1040 MIRA) as shown in Fig. 2. The MIRA device consists of an array of dry point contact (DPC) transducers that emit ultrasonic waves into concrete structures and records the response. It has 48 transducers arranged in a 4 × 12 array at 3 cm spacing, with the transducers acting as transmitters and receivers in a sequential mode. Since the signal ray path is controlled by the transducer polarization, measurements were conducted along two directions: lateral (X) direction and longitudinal (Y) direction as shown in Fig. 2a. Five parallel survey lines at 200 mm spacing were used for each direction as shown Fig. 1b (lines 1–5 for x-scan and lines A-E for y-scan). The MIRA device was moved along these survey lines (device center on the lines), and data were sampled for 51 scan points at 20 mm spacing for each line. A total of 255 scan points (5 × 51) were collected for each direction. For each scan point, a total of 66 measurements (time-history channels) were recorded for the total recording time of 0.6 millisecond with a sampling rate of 1 microsecond.

3.1. Analysis of a sample dataset

Analysis of a sample dataset is presented in detail to illustrate the SH-FWI method. The data were collected at the marked grid as shown in Fig. 2a and b for the top and side views, respectively. It is noted that the small shallow delamination shown in Fig. 1a (upper, left) was under the pictured sampling point in Fig. 2a. In addition, this scan area covered

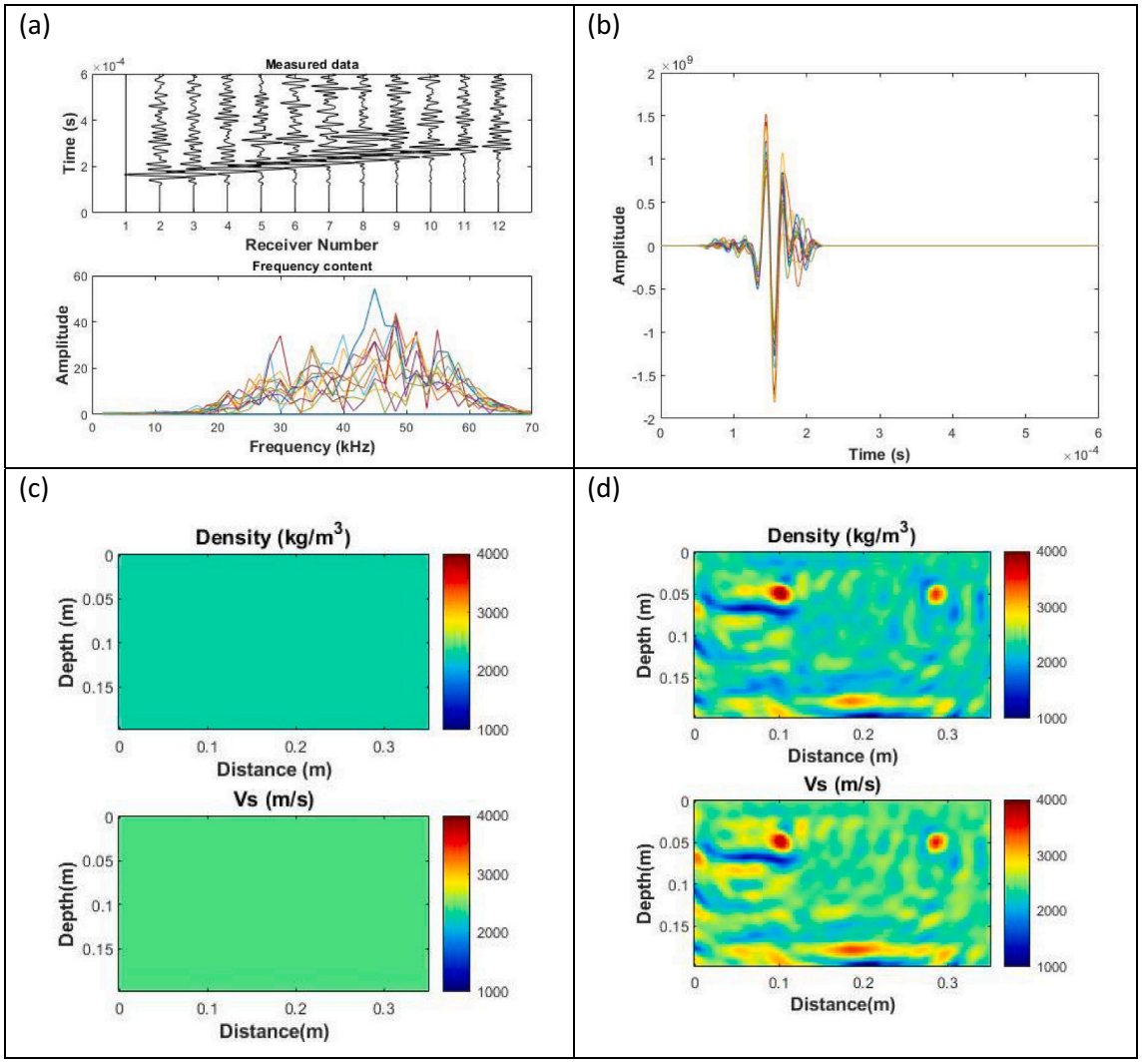

Fig. 3. Experiment: (a) the measured waveform and frequency distribution, (b) the estimated source signatures associated with the initial model, (c) the homogenous initial model based on measured Vs and density of concrete, and (d) final inverted result.

four rebars in two layers as shown in Fig. 2b. The measured ultrasonic data were filtered through the frequency bandwidth of 20 to 70 kHz before analysis. The data beyond this selected frequency range were not consistent and thus removed from analysis. Fig. 3a shows the filtered data (upper) induced by the first row of transducers, and the corresponding spectra (bottom) with the central frequency of around 45 kHz.

For inversion, the dimension of medium was selected as 350 mm × 200 mm (length × depth). The selected length was determined by the size of MIRA device that has the grid length of 330 mm (11 spaces of 30 mm), and 10 mm spacing was added in each side. The inverted depth was defined as 200 mm, which is 10 mm deeper than the true thickness of concrete slab. The perfectly matched layers (PML) were applied at the bottom and two vertical boundaries of the medium to absorb outgoing waves of simulated wavefields. The PMLs were implemented by extending the numerical grid beyond the modelled domain, and each extended grid has the same values of Vs and density of cells along the edge of the modelled domain. This approach has two advantages. First, the true thickness of slab is not required for analysis and can be interpreted from the inverted result. Specifically, the analyzed domain is thicker than the lab, and Vs and density are inverted for the entire domain to infer the back-wall. Second, PML eliminates the need to predefine the free surface condition at the bottom boundary in the forward simulation, which makes the application more flexible. During the inversion, the medium was discretized into 2 × 2-mm cells for both the forward modelling and model updating. The cell size of 2 mm was selected to achieve at least 10 grid points per minimum wavelength for accurate wave simulation and to provide a high-resolution inverted image.

During the inversion, the source estimation was used to simulate the true source signature, see [39,48] for the detailed implementation. The source signature was estimated and updated at the beginning of each iteration due to the updated model parameters. Fig. 3b presents the estimated source signatures for all rows of transmitters associated with the initial model. Their similarity of phase and amplitude indicates the consistency of wave energy generated by the MIRA device. In addition, a calibration function [49] was applied to the estimated data to account for the attenuation due to material damping:

$$y(r) = Ar^{\alpha} \tag{14}$$

where r represents the source-receiver offset. The factor A and exponent α are constants, and they were determined by minimizing the energy of waveform residuals. Specifically, for each source-receiver offset, the maximum waveform amplitudes were averaged from all source-receiver pairs having the same offset to develop the amplitude-offset curve (AOC). The AOC of the estimated data was matched with that of the measured data to determine A and α. The calibration function $y(r)$ represents the average wave attenuation along the entire length of the

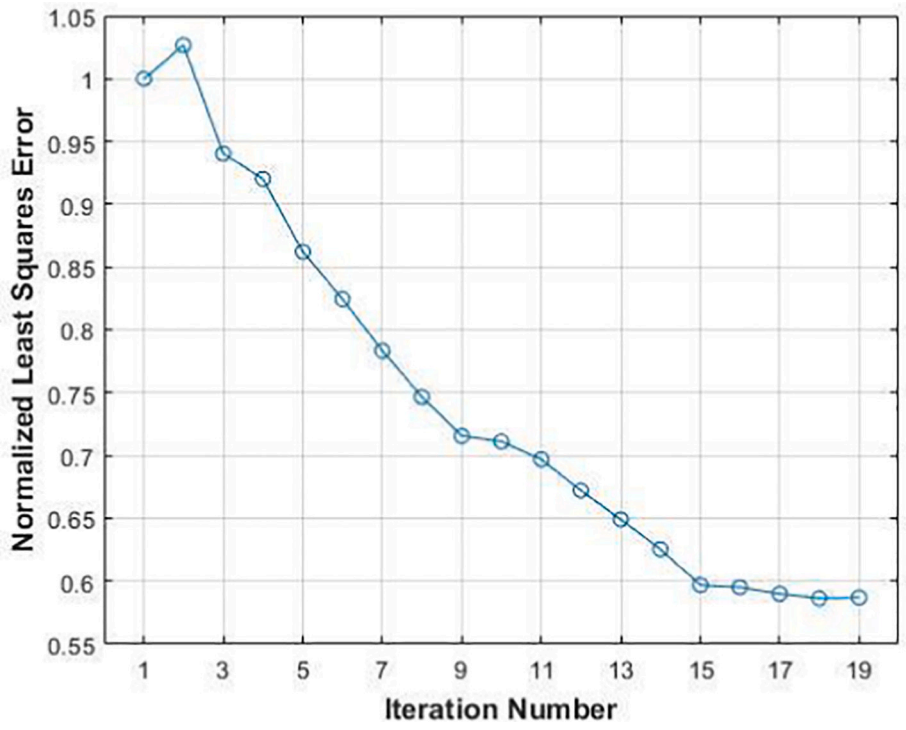

Fig. 4. Normalized least-squares error versus the iteration number.

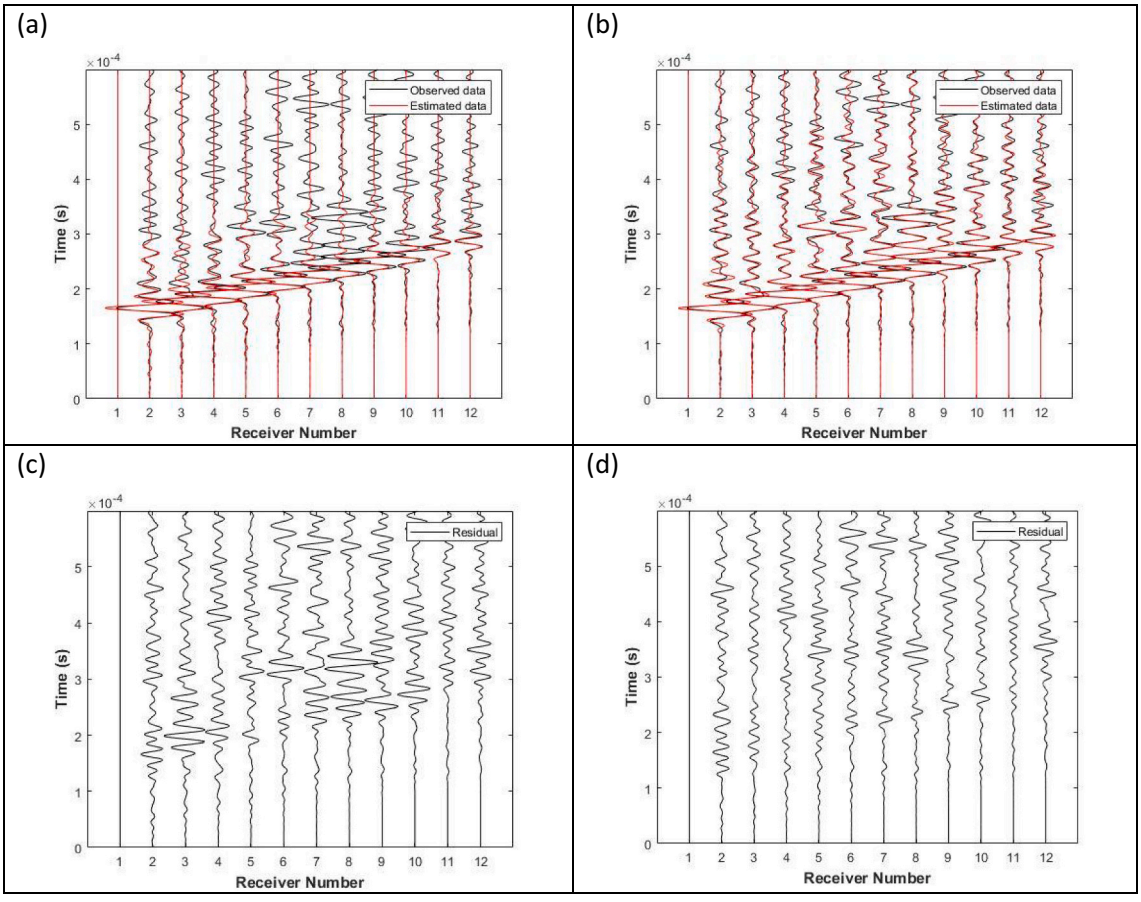

Fig. 5. Waveform comparison: (a) observed data and estimated data from the initial model, (b) observed data and estimated data from the final inverted model, (c) initial residual associated with the initial model, and (d) final residual associated with the final inverted model.

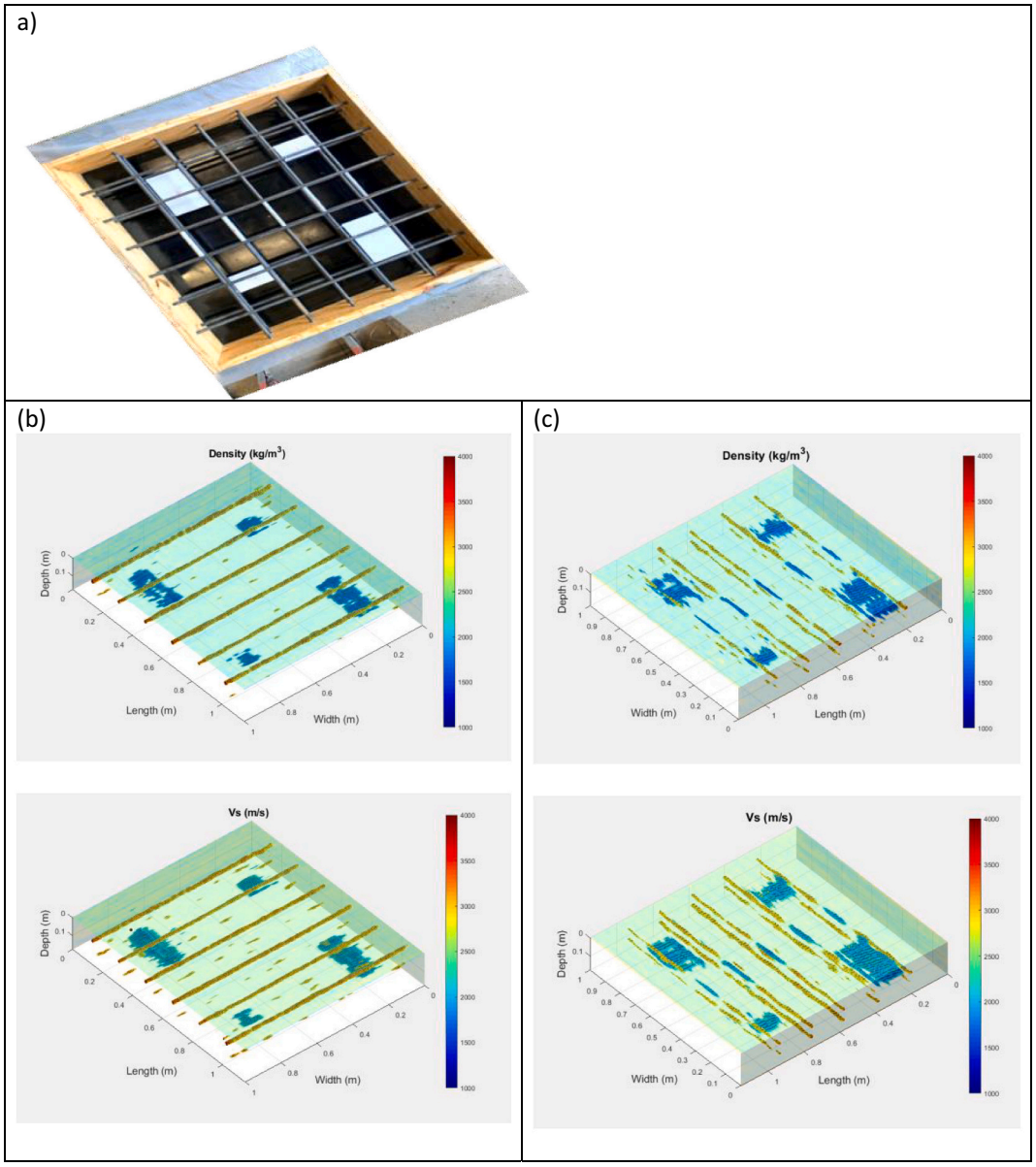

Fig. 6. The 3D view comparison: (a) true delamination and rebars, (b) inverted density (upper) and Vs (bottom) from y-scan, and (c) inverted density (upper) and Vs (bottom) from x-scan.

transducer array. It was determined at the beginning of each run and kept constant during inversion.

To avoid the cycle skipping problem (matching of wrong waveform peaks), an appropriate initial model needs to be determined at the beginning of inversion. For Vs, the initial model was determined through the MIRA device measurement. The device built-in software calculated Vs at each sample location using the SH-wave arrival times (peak to peak) across all transducers. The Vs values from eight random locations on the surface of concrete slab were measured by the MIRA device, given the various values from 2460 to 2550 m/s. Therefore, the initial model was selected as a homogenous model with the averaged Vs value of 2500 m/s (Fig. 3c, bottom). When the slab was cast, three concrete cylinder specimens were made to determine the initial density model. The average density value obtained from the cylinder specimens was around 2300 kg/m^3, which was then chosen as the initial model for density (Fig. 3c, top).

The density and Vs models were updated simultaneously and independently during inversion. The stopping criteria were setup as that the predefined maximum iterations of 30 was reached or no better model was found. The inversion stopped after 19 iterations and took approximately 9 min on a desktop computer (Dell Precision, 40 cores of 2.0 GHz each, 1.0 TB RAM). The least-squares error for all 19 iterations is shown in Fig. 4. The error decreased gradually from 1.0 at the beginning to around 0.6 in the final iteration.

Fig. 5a and b compare the measured data and estimated data associated with the initial model and final inverted model, respectively. The residuals corresponding to the initial model and final inverted model are shown in Fig. 5c and d, respectively. There are significant residuals at the beginning of inversion (Fig. 5c), since no reflection of rebar, delamination, and bottom boundary is generated from the initial model. As those objects were reconstructed during inversion, the waveform match improved (Fig. 5a to b), and the residuals decreased significantly for most channels (Fig. 5c to d). The measured and estimated waveform data agree well, both have similar phases and magnitudes for all channels at the end of inversion (Fig. 5b).

The final inverted results are shown in Fig. 3d for Vs and density. Compared to the initial model (Fig. 3c), the Vs and density changed significantly during inversion. The delamination is characterized at its

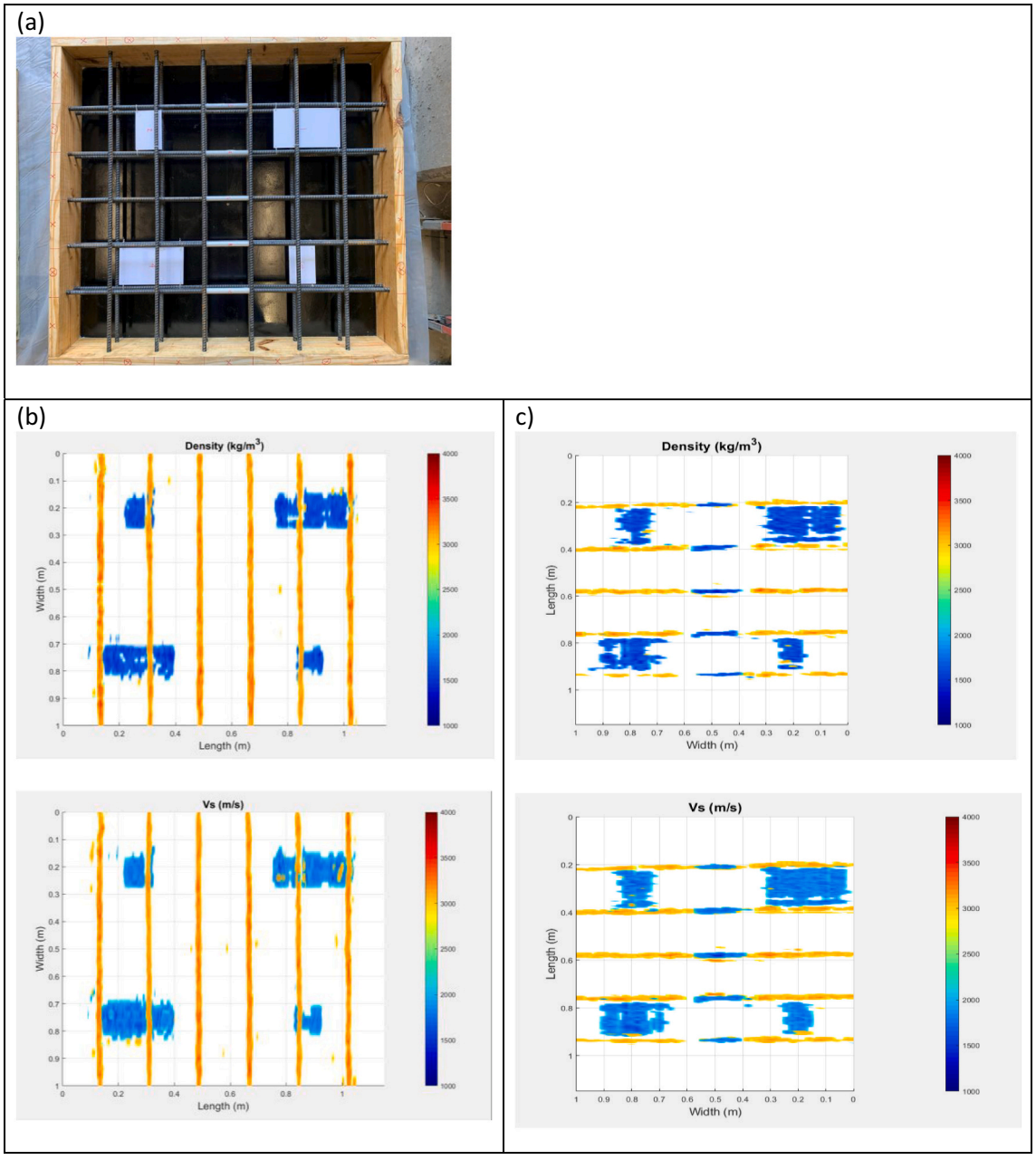

Fig. 7. The plan view comparison: (a) true delamination and rebars, (b) the inverted density (upper) and Vs (bottom) from y-scan, (c) inverted density (upper) and Vs (bottom) from x-scan.

true location (depth 65 mm, distance 0.02–0.12 m). It has the inverted Vs value of 1000–1300 m/s and density value of 1100–1300 kg/m^3. It is noted that the inverted thickness of delamination (3 cells of 6 mm) is thicker than the true thickness (3 mm). This is due to the smoothing effect caused by the regularization, which led to the blurred top and bottom edges of delamination. Two top rebars are clearly imaged in both density and Vs models at the true locations (Fig. 2b). The rebars have Vs value of 3200–3500 m/s and the density value of 3500–4000 kg/m^3. The inverted Vs value of rebar is close to the true Vs of steel, which is typically around 3250 m/s. However, the inverted density value is lower than the true density of steel, which should be around 7800 kg/m^3. This is because the initial density was too far away from the steel density, and the applied Tikhonov regularization smoothed the gradient that led to constrained parameter updating. The two bottom rebars are not imaged for this sampled location, as the reflections from these rebars are partly blocked by the delamination and mixed with those from the back-wall. Lastly, the concrete-air interface at the back-wall is imaged at a depth of about 0.19 m from the surface, showing good agreement with the true thickness of concrete slabs.

3.2. Complete 3D result of the whole concrete slab

All collected datasets were analyzed with the same procedure as illustrated in the previous section. The individual results were first combined into 2D cross-sections and then a 3D image. Each 2D cross-section was created by combing the inverted results from five successive scans at 200 mm sampling intervals. Because the length of the analyzed medium (350 mm) for each scan is larger than the sampling interval (200 m), there is a 150 mm overlap between two adjacent scan areas. The density and Vs values within this overlap were taken as the average of the two corresponding values. The averaging helped to mitigate some inversion artifacts and enhance images of delamination

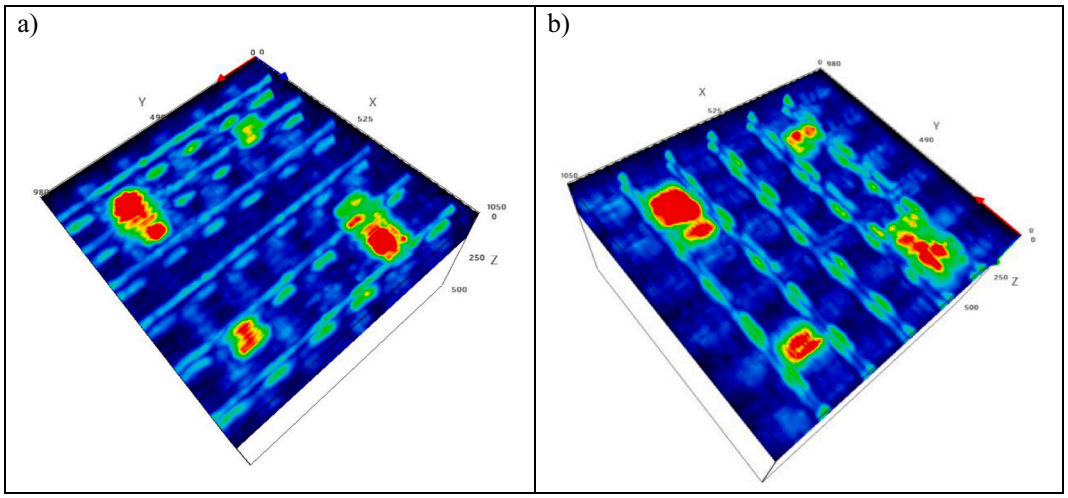

Fig. 8. Ultrasonic images processed by the MIRA built-in software based on 2D SAFT: a) y-scan and b) x-scan.

and rebars. The 2D cross-sections were then combined into a 3D image of the whole concrete slab.

The rendering of 3D result images is shown in Fig. 6b and c for y-scan (longitudinal) and x-scan (lateral), respectively, together with the formwork photo (Fig. 6a). For both y-scan and x-scan, the 3D image has the length of 1150 mm, width of 1000 mm, and the depth of 180 mm. The length of 3D image is determined by the length of each combined 2D cross-section. The width is determined by the length of each survey line, which has 51 points and the interval spacing of 20 mm. The depth of 180 mm (less than the slab thickness) was used to remove the back-wall image for better viewing of defects. For rendering, the transparency level with various density and Vs scales were selected. For the high-value cells (e.g., rebars), Vs values larger than 3200 m/s and density values larger than 3500 kg/m^3 were selected to be shown as opaque. For the low-value cells (e.g., delamination, debonding of rebar), Vs value less than 1300 m/s and density value less than 1300 kg/m^3 were selected to be shown as opaque. The remaining cells were shown as transparent for viewing of the entire model.

The 3D images (Fig. 6b and c) clearly show the rebars and defects in both density model (top) and Vs model (bottom). In both x-scan and y-scan images, all four delaminations are well characterized with accurate depths and horizontal dimensions (width and length). However, the thicknesses of delaminations cannot be distinguished due the adopted regularization that smoothed the concrete-delamination contrast. In the y-scan image (Fig. 6b), the top layer of six shallowest rebars is well reconstructed, while the deepest layer of rebars is partly identified due to the weak signal coverage. In the x-scan image (Fig. 6c), the two layers of rebars are identified. The top layer of rebars is imaged clearer than the bottom layer of rebars due to stronger signal coverage. In addition, the rebar images have some discontinuities at rebar intersect locations. This is due to the signal blocking from the shallower transverse rebars.

The rebar debonding is imaged at the middle section (blue section) of each rebar in both density and Vs images (Fig. 6c). The rebar debonding sections are clearly distinguished from the regular rebar sections. This is attributed to that the FWI uses the entire recorded data and matches positive and negative magnitudes separately in time domain. As the reflections from rebar debonding and regular rebars often have different phases (or signs of magnitudes), and matching positive and negative magnitudes separately helps to distinguish reflections from a low-velocity zone (debonding) and a high-velocity zone (regular rebar). It is noted that the debonding is characterized as low-density and low-velocity cells for the entire rebar cross-section, regardless of debonding levels. This is due to wave signal reflection at the outer boundary of debonding layers that does not allow propagation through the debonding layer into rebars. Nevertheless, the successful detection of the debonding is particularly important for assessments of rebar-concrete bonding, load transfer, and structural durability.

For further assessment, the plan views of SH-FWI results are shown in Fig. 7, together with the formwork photo. Again, all four delaminations are characterized with accurate dimensions. The two shallow delaminations (Fig. 7a, upper left and right) are better imaged than the two deeper ones (Fig. 7a, bottom left and right). The rebars in both directions are imaged at their true locations. The rebar debonding sections are identified and distinguished from the regular sections (Fig. 7c).

For comparison, the same collected ultrasonic datasets were analyzed by the MIRA built-in software, which is based on the 2D SAFT [40]. Individual 2D images are then combined into a 3D image using the "IntroView" software provided by the MIRA manufacturer. Fig. 8a and b show the reconstructed 3D images for the y-scan and x-scan, respectively. In the y-scan image, the six shallow rebars and four delaminations are imaged. Similar to the SH-FWI result, only parts of the six deeper rebars in y-scan are reconstructed due to the weak signal coverage. In the x-scan image, the two layers of rebars and four delaminations are imaged. Unlike the SH-FWI, the built-in SAFT was not able to image the rebar debonding. This can be explained by that the SAFT image at a cell is computed as a sum of absolute magnitudes of recorded data at a flight time (travel time from a source to the cell plus travel time from the cell to a receiver), and negative and positive magnitudes have the same effect. As the reflections from rebar debonding and regular rebars often have similar absolute values, the SAFT cannot distinguish them.

The main advantage of the SH-FWI method over the SAFT is that the SH-FWI can provide the material properties (density and Vs) at mm-resolutions for comprehensive assessment of structure integrity, damage, and durability. Knowing both density and Vs, the shear modulus can be computed for subsequent engineering analyses (concrete strength, stress-strain, load-deformation). More importantly, the SH-FWI can characterize the high and low-velocity anomalies for assessment of deterioration levels. The SAFT can only provide the reflection images and cannot distinguish high- and low-velocity objects (e.g., both rebars and delaminations shown as red zones in Fig. 8). It is worth to note that the SAFT method requires much less computing time, and thus it remains the efficient and robust method for real-time inspection.

The future work will be the application of this 2D SH-FWI method on field data with more challenging scenarios such as irregular, thin or water-filled delamination/cracks. As the method worked well for field data on soil/rock with thin soil layer, irregular soil zones, water-filled anomalies [39], it is expected to work well for these field scenarios of concrete structures. As it characterizes material properties (Vs and density) in mm-cells, the irregular or thin (>1–2 mm), or water-filled delamination should be imaged. However, field experiment is needed

to confirm. Nevertheless, the presented results from the laboratory settings show the excellent capabilities of the method in detection of delamination and rebar debonding, and its superiority over the conventional SAFT.

4. Conclusions

The first-time application of 2D SH-FWI method is presented for detection of delamination and rebar debonding in concrete structures. The method was evaluated on a fabricated concrete slab with artificial delamination areas and rebar debonding. The ultrasonic SH-wave datasets were collected by a shear-wave tomography equipment (A1040 MIRA) and analyzed to build 2D cross-sections, which are then combined into a 3D representation. The method can characterize all four delaminations with accurate depths (65 and 130 mm) and dimensions (100 × 150 and 250 × 150 mm), as well as rebar debonding. Compared to the built-in MIRA software based on the SAFT, which cannot identify rebar debonding, the SH-FWI clearly distinguished the rebar debonding sections from the regular rebar sections. This is explained by that the reflections from debonding and regular rebars often have similar absolute magnitudes but different phases (or signs of magnitudes). Unlike the SAFT uses the absolute magnitudes in constructing images, the SH-FWI matches positive and negative magnitudes separately and thus be able to distinguish the regular and debonding rebars. Although the SH-FWI method requires more computer time for data processing, it is an efficient tool for targeted, in-depth inspection of concrete structures. The method can provide the material properties (density and Vs) at high resolution for comprehensive assessment of structure integrity, damage, and durability, as well as for subsequent engineering analyses such as concrete strength (moduli), stress-strain, and load-deformation behaviors.

Declaration of Competing Interest

The authors declare that they have no known competing financial interests or personal relationships that could have appeared to influence the work reported in this paper.

The authors declare the following financial interests/personal relationships which may be considered as potential competing interests.

References

[1] P.D. Cady, E.J. Gannon, Condition Evaluation of Concrete Bridges Relative to Reinforcement Corrosion, Strategic Highway Research Program, Washington, D.C., 1993. ISBN: 309-05258-0.

[2] N. Gucunski, A. Imani, F. Romero, S. Nazarian, D. Yuan, H. Wiggenhauser, P. Shokouhi, A. Taffe, D. Kutrubes, Nondestructive Testing to Identify Concrete Bridge Deck Deterioration, Transportation Research Board, Washington, D.C., 2013. ISBN: 978-0-309-12933-6.

[3] F. Wu, F.-K. Chang, Debond detection using embedded piezoelectric elements in reinforced concrete structures – part I: experiment, Struct. Health Monit. 5 (1) (2006) 5–15, https://doi.org/10.1177/1475921706057978.

[4] M. Scott, A. Rezaizadeh, M. Moore, Phenomenology Study of HERMES Ground-penetrating Radar Technology for Detection and Identification of Common Bridge Deck Features, No. FHWA-RD-01-090, 2001.

[5] K. Dinh, N. Gucunski, K.T. Tran, A. Novo, T. Nguyen, Full-resolution 3D imaging for concrete structures with dual-polarization GPR, Autom. Constr. 125 (2021) 103652, https://doi.org/10.1016/j.autcon.2021.103652.

[6] A.A. Sultan, G.A. Washer, Reliability analysis of ground-penetrating radar for the detection of subsurface delamination, J. Bridg. Eng. 23 (2) (2017), 0417131, https://doi.org/10.1061/(ASCE)BE.1943-5592.0001182.

[7] S. Yehia, O. Abudayyeh, S. Nabulsi, I. Abdelqader, A comparison between Ground Penetrating Radar (GPR) and Impact Echo (IE) for detection of common concrete bridge decks defects, in: International Conference on Computing in Civil Engineering 2005. Cancun, Mexico, 2005, https://doi.org/10.1061/40794(179)34.

[8] D6087-08, ASTM, Standard Test Method for Evaluating Asphalt-Covered Concrete Bridge Decks Using Ground Penetrating Radar, ASTM International, 2015. http://www.astm.org/cgi-bin/resolver.cgi?D6087-08(2015)e1.

[9] N. Gucunski, G.R. Consolazio, A. Maher, Concrete bridge deck delamination detection by integrated ultrasonic methods, Int. J. Mater. Prod. Technol. 26 (1/2) (2006) 19–34, https://doi.org/10.1504/IJMPT.2006.008978.

[10] H. Azari, D. Yuan, S. Nazarian, N. Gucunski, Sonic methods to detect delamination in concrete bridge decks: impact of testing configuration and data analysis approach, J. Transp. Res. Board 2292 (2012) 113–124, https://doi.org/10.3141/2292-14.

[11] P. Shokouhi, J. Wöstmann, G. Schneider, B. Milmann, A. Taffe, H. Wiggenhauser, Nondestructive detection of delamination in concrete slabs: multiple-method investigation, J. Transp. Res. Board 2251 (1) (2011) 103–113, https://doi.org/10.3141/2251-11.

[12] N.J. Carino, The Impact-Echo method: An overview, in: Proceedings of the 2001 Structures Congress & Exposition, Washington, D.C, 2001. https://tsapps.nist.gov/publication/get_pdf.cfm?pub_id=860355.

[13] N. Gucunski, B. Pailes, J. Kim, H. Azari, K. Dinh, Capture and quantification of deterioration progression in concrete bridge decks through periodical NDE surveys, J. Infrastruct. Syst. 23 (1) (2017), B4016005, https://doi.org/10.1061/(ASCE)IS.1943-555X.0000321.

[14] J.S. Popovics, J.R. Roesler, J. Bittner, A.N. Amirkhanian, A.S. Brand, P. Gupta, K. Flowers, Ultrasonic Imaging for Concrete Infrastructure Condition Assessment and Quality Assurance, Illinois Center for Transportation, 2017. https://www.ideals.illinois.edu/handle/2142/95.

[15] P. Shokouhi, J. Wolf, H. Wiggenhauser, Detection of delamination in concrete bridge decks by joint amplitude and phase analysis of ultrasonic array measurements, J. Bridg. Eng. 19 (3) (2014), 04013005, https://doi.org/10.1061/(ASCE)BE.1943-5592.0000513.

[16] K. Dinh, N. Gucunski, Factors affecting the detectability of concrete delamination in GPR images, Constr. Build. Mater. 274 (8) (2021) 121837, https://doi.org/10.1016/j.conbuildmat.2020.121837.

[17] J. Virieux, S. Operto, An overivew of full-waveform inversion in exporation geophysics, Geophysics 74 (6) (2009), https://doi.org/10.1190/1.3238367, 1ND-Z107.

[18] R. Pratt, Seismic waveform inversion in the frequency domain, part 1: theory and verification in a physical scale model, Geophysics. 64 (3) (1999) 888–901, https://doi.org/10.1190/1.1444597.

[19] R.M. Shipp, S.C. Singh, Two-dimensional full wavefield inversion of wide-aperture marine seismic streamer data, Geophys. J. Int. 151 (2) (2002) 325–344, https://doi.org/10.1046/j.1365-246X.2002.01645.x.

[20] D.H. Sheen, K. Tuncay, C.E. Baag, P. Ortoleva, Time-domain gauss-Newton seismic waveform inversion in elastic media, Geophys. J. Int. 167 (3) (2006) 1373–1384, https://doi.org/10.1111/j.1365-246X.2006.03162.x.

[21] L. Métivier, F. Bretaudeau, R. Brossier, S. Operto, J. Virieux, Full waveform inversion and the truncated Newton method: quantitative imaging of complex subsurface structures, Geophys. Prospect. 62 (6) (2014) 1353–1375, https://doi.org/10.1111/1365-2478.12136.

[22] K.T. Tran, M. Mcvay, M. Faraone, D. Horhota, Sinkhole detection using 2D full seismic waveform tomography, Geophysics. 78 (5) (2013) R175–R183, https://doi.org/10.1190/geo2013-0063.1.

[23] I. Epanomeritakis, V. Akçelik, O. Ghattas, J. Bielak, A Newton-CG method for large-scale three-dimensional elastic full-waveform seismic inversion, Inverse Problems. 24 (2008), 034015, https://doi.org/10.1088/0266-5611/24/3/034015.

[24] A. Fichtner, B.L.N. Kennett, H. Igel, H.P. Bunge, Full seismic waveform tomography for upper-mantle structure in the Australasian region using adjoint methods, Geophys. J. Int. 179 (3) (2009) 1703–1725, https://doi.org/10.1111/j.1365-246X.2009.04368.x.

[25] C. Tape, Q. Liu, A. Maggi, J. Tromp, Seismic tomography of the southern California crust based on spectral-element and adjoint methods, Geophys. J. Int. 180 (1) (2010) 433–462, https://doi.org/10.1111/j.1365-246X.2009.04429.x.

[26] L. Métivier, R. Brossier, Q. Mérigot, E. Oudet, J. Virieux, An optimal transport approach for seismic tomography: application to 3D full waveform inversion, Inverse Problems. 32 (11, 2016) 115008, https://doi.org/10.1088/0266-5611/32/11/115008.

[27] M. Majid, K.T. Tran, M. Mcvay, D. Horhota, S.J. Wasman, Sinkhole detection with 3D full seismic waveform tomography, Geophysics. 85 (5) (2020) B169–B179, https://doi.org/10.1190/geo2019-0490.1.

[28] J. Rao, M. Rarassepp, Z. Fan, Limited-view ultrasonic guided wave tomography using an adaptive regularization method, J. Appl. Phys. 120 (2016) 194902, https://doi.org/10.1063/1.4967790.

[29] L.T. Nguyen, R.T. Modrak, Ultrasonic wavefield inversion and migration in complex heterogenous structures: 2D numerical imaging and nondestructive testing experiments, Ultrasonics. 82 (2018) 357–370, https://doi.org/10.1016/j.ultras.2017.09.011.

[30] D. Köhn, T. Meier, M. Fehr, D.D. Nil, M. Auras, Application of 2D elastic Rayleigh waveform inversion to ultrasonic laboratory and field data, Near Surface Geophys. 14 (5) (2016) 461–467, https://doi.org/10.3997/1873-0604.2016027.

[31] F. Jalinoos, K.T. Tran, T.D. Nguyen, A.K. Agrawal, Evaluation of bridge abutments and bounded wall type structures with ultraseismic waveform tomography, J. Bridg. Eng. 22 (12, 2017), 0417104, https://doi.org/10.1061/(ASCE)BE.1943-5592.0001150.

[32] K.T. Tran, F. Jalinoos, T.D. Nguyen, A.K. Agrawal, Evaluation of bridge abutment with Ultraseismic waveform tomography: field data application, J. Nondestruct. Eval. 38 (4) (2019) 1–13, https://doi.org/10.1007/s10921-019-0631-4.

[33] T.D. Nguyen, K.T. Tran, N. Gucunski, Detection of bridge-deck delamination using full ultrasonic waveform tomography, J. Infrastruct. Syst. 23 (2) (2017), 04016027, https://doi.org/10.1061/(ASCE)IS.1943-555X.0000323.

[34] J. Xia, Y. Xu, Y. Luo, R.D. Miller, R. Cakir, C. Zeng, Advantages of using multichannel analysis of love waves (MALW) to estimate near-surface shear-wave velocity, Surv. Geophys. 33 (5) (2012) 841–860, https://doi.org/10.1007/s10712-012-9174-2.

[35] Y. Pan, J. Xia, Y. Xu, L. Gao, Z. Xu, Love-wave waveform inversion in time domain for shallow shear-wave velocity, Geophysics. 81 (1) (2016) R1–R14, https://doi.org/10.1190/geo2014-0225.1.
[36] E. Dokter, D. Köhn, D. Wilken, D. De Nil, W. Rabbel, Full waveform inversion of SH- and love-wave data in near-surface prospecting, Geophys. Prospect. 65 (S1) (2017) 216–236, https://doi.org/10.1111/1365-2478.12549.
[37] F. Wittkamp, N. Athanasopoulos, T. Bohlen, Individual and joint 2-D elastic full-waveform inversion of Rayleigh and love waves, Geophys. J. Int. 216 (1) (2019) 350–364, https://doi.org/10.1093/gji/ggy432.
[38] R. Chen, K.T. Tran, 2D gauss-Newton full waveform inversion of SH- and love-waves in the time domain, J. Appl. Geophys. 191 (2021) 104363, https://doi.org/10.1016/j.jappgeo.2021.104363.
[39] R. Chen, K.T. Tran, Y. Wang, 2D time-domain full-waveform inversion of SH- and love-waves for geotechnical site characterization, Near Surf. Geophys. 19 (3) (2021) 283–295, https://doi.org/10.1002/nsg.12137.
[40] M. Schickert, M. Krause, W. Müller, Ultrasonic imaging of concrete elements using reconstruction by synthetic aperture focusing technique, J. Mater. Civ. Eng. 15 (3) (2003) 235–246, https://doi.org/10.1061/(ASCE)0899-1561(2003)15:3(235).
[41] J. Virieux, SH-wave propagation in heterogenous media: velocity-stress finite-difference method, Geophysics. 49 (11, 1984) 1933–1942, https://doi.org/10.1190/1.1441605.
[42] A.R. Levander, Fourth-order finite-difference P-SV seismograms, Geophysics. 53 (11, 1988) 1425–1436, https://doi.org/10.1190/1.1442422.
[43] D. Komatitsch, R. Martin, An unsplit convolutional perfectly matched layer improved at grazing incidence for the seismic wave equation, Geophysics. 72 (5) (2007) SM155–SM167, https://doi.org/10.1190/1.2757586.
[44] R.-E. Plessix, A review of the adjoint-state method for computing the gradient of a functional with geophysical applications, Geophys. J. Int. 167 (2) (2006) 495–503, https://doi.org/10.1111/j.1365-246X.2006.02978.x.
[45] A.N. Tikhonov, V.Y. Arsenin, Solutions of Ill-posed Problems, V.H. Winston & Sons, Washington D.C., 1977.
[46] J. Nocedal, S.J. Wright, Numerical Optimization, Springer, New York, 2006. ISBN-10: 0-387-30303-0.
[47] Z. Zhang, L. Huang, Y. Lin, Double-Difference Elastic-Waveform Inversion with Weighted Gradients for Monitoring EGS Reservoirs. In: Thirty-Seventh Workshop on Geothermal Reservoir Engineering, Stanford University, Stanford, California, 2012.
[48] S. Busch, J.V.D. Kruk, J. Bikowski, H. Vereecken, Quantitative conductivity and permittivity estimation using full-waveform inversion of on-ground GRP data, Geophysics 77 (6) (2012) H79–H91, https://doi.org/10.1190/geo2012-0045.1.
[49] M. Schäfer, L. Groos, T. Forbriger, T. Bohlen, On the effects of geometrical spreading corrections for a 2D full waveform Inversion of recorded shallow seismic surface waves, in: 74th EAGE conf. and Exhibition incorporating SPE EUROPEC, European Association of Geoscientists & Engineers, 2012. ISBN: 978-0-470-99124-4.